Applied Catalysis B: Environmental 156–157 (2014) 173–183

Contents lists available at ScienceDirect

Applied Catalysis B: Environmental

journal homepage: www.elsevier.com/locate/apcatb

Enhanced photocatalytic activity of homoassembled ZnO nanostructures on electrospun polymeric nanofibers: A combination of atomic layer deposition and hydrothermal growth

Fatma Kayaci[a,b], Sesha Vempati[a,*], Cagla Ozgit-Akgun[a,b], Necmi Biyikli[a,b], Tamer Uyar[a,b,**]

[a] UNAM-National Nanotechnology Research Center, Bilkent University, Ankara, 06800, Turkey
[b] Institute of Materials Science and Nanotechnology, Bilkent University, Ankara, 06800, Turkey

ARTICLE INFO

Article history:
Received 10 December 2013
Received in revised form 24 February 2014
Accepted 4 March 2014
Available online 14 March 2014

Keywords:
Photocatalysis
ZnO
Electrospinning
Atomic layer deposition
Hydrothermal

ABSTRACT

We report on the synthesis and photocatalytic activity (PCA) of electrospun poly(acrylonitrile) (PAN) nanofibrous mat decorated with nanoneedles of zinc oxide (ZnO). Apart from a detailed morphological and structural characterization, the PCA has been carefully monitored and the results are discussed elaborately when juxtaposed with the photoluminescence. The present hierarchal homoassembled nanostructures are a combination of two types of ZnO with diverse optical qualities, i.e. (a) controlled deposition of ZnO coating on nanofibers with dominant oxygen vacancies and significant grain boundaries by atomic layer deposition (ALD), and (b) growth of single crystalline ZnO nanoneedles with high optical quality on the ALD seeds via hydrothermal process. The needle structure (~25 nm in diameter with an aspect ratio of ~24) also supports the vectorial transport of photo-charge carriers, which is crucial for high catalytic activity. Furthermore, it is shown that enhanced PCA is because of the catalytic activity at surface defects (on ALD seed), valence band, and conduction band (of ZnO nanoneedles). PCA and durability of the PAN/ZnO nanofibrous mat have also been tested with aqueous solution of methylene blue and the results showed almost no decay in the catalytic activity of this material when reused.

1. Introduction

Photocatalysis is one of the widely researched [1–11] topics because of its importance in water and environmental purification in the background of unavoidable and ever increasing industrialization [12]. Photocatalysts (PCs) are generally nanostructured semiconductors which are employed either directly [1,2,5,10], doped format [7], defect-induced [3,4,13–15] or combined with another material to yield a synergy effect. Such combinations exploit plasmonic effect [6] or properties of other semiconductors [7–9,11] depicting relatively higher photocatalytic activity (PCA) than their pristine counterparts. Despite the higher PCA those combinations also increase the complexity of the process and at the end they should be compatible with the environment [10]. Metal-doped semiconductors can be unstable and corrode after long term usage causing a gradual decay in the PCA [12], apart from the difficulties in their preparation and characterization [16]. Of course this does not apply to noble metals [17] which are stable in the context of photo-oxidation; on the other hand, if Au nanoparticles are larger than a critical size, then they may act as e/h recombination centers which reduce the PCA [17]. In any case, the main aim is to engineer a PC possessing enhanced PCA as well as stability over a decent period of time.

Among a list of semiconductors employed in photocatalysis, ZnO nanostructures have attracted a lot of attention [1,2,4–6,15,18] due to their easy processability via a variety of methods [5,19–21], versatility in nanostructuring [5,19–21], non-toxicity, abundance, low cost, etc. Having listed the properties which make the nanostructured-ZnO a highly suitable candidate as a PC, we should agree with the fact that ideally defect-free-ZnO can use only UV region (3–4%) of the solar spectrum because of its wider band gap and therefore 44–47% of visible light is left unused. Hence, it obviously is a wise choice to harness the visible as well as UV region of solar energy to achieve significantly higher PCA. We also note that the morphology and crystal structure of ZnO at nanoscale are detrimental on various properties including optical [15,19–21],

* Corresponding author. Tel.: +90 3122903533.
** Corresponding author. Tel.: +90 3122903571.
E-mail addresses: svempati01@qub.ac.uk (S. Vempati), tamer@unam.bilkent.edu.tr, tameruyar@gmail.com (T. Uyar).

http://dx.doi.org/10.1016/j.apcatb.2014.03.004
0926-3373/

photostability [22,23] and PCA [14,15,24]. In order to initiate or improve the light absorption in the visible region one can engage the native defects of ZnO [13,15], which form sub-band gap states [21]. For example, oxygen vacancies (V_Os) are induced in ZnO and recently shown to improve PCA [3,4,25], alongside of other similar studies [13–15]. On the other hand, V_Os not only create intermediate bands, but also act as self-dopants and induced bandgap reduction [25]. Therefore, by considering the various properties of nanostructured-ZnO, it is convincing and logical to design a smart and efficient ZnO catalyst depicting high PCA is of fundamental as well as technological importance. Here we demonstrate a novel hybrid approach, in which we combine chemical vapor deposition (CVD) and liquid phase deposition (LPD) techniques. Atomic layer deposition (ALD) and hydrothermal growth are combined to fabricate a hierarchy of nanostructured-ZnO on electrospun poly(acrylonitrile) (PAN) nanofibers. The resulting ZnO nanostructures depict synergy effect and show enhanced PCA. PAN nanofibers are well adoptable in water filtration where their unique properties such as high surface area, nanoporous structure, low basis weight, easy permeability, good stability and chemical resistance are worth mentioning [26–29]. In our previous study [2] electrospun polymeric nanofibers were subjected to varying ALD parameters where we have studied how the PCA is influenced when nanoparticles transform into continuous film. We had inferred that highly dense nanoparticles show relatively higher PCA due to the increased surface area consisting of oxygen vacancy and other related defects. We believe that having polycrystalline film alone is not adequate to yield high PCA, hence in this study, we have grown single crystalline ZnO nanoneedles on the ALD-seed coating. Note that the single crystalline ZnO nanoneedles can depict the lowest possible defect density. Furthermore, previous studies [3,4,13–15,25] have introduced V_Os throughout the catalyst, however, in contrast we have combined two materials one of which is dominant in oxygen related defects, while the other is virtually defect-free single crystal. We also show that the present combination yields enhanced PCA in the presence of high aspect ratio ZnO nanoneedles with an average diameter and length of ~25 nm and ~600 nm, respectively. We note that surface area to volume ratio cannot equivalently improve the PCA [10] whereas one dimensional semiconductors have already shown to depict vectorial transport of photogenerated charge carriers and helping to improve the PCA [30,31]. While maintaining a delicate balance between the advantages [13–15,25] and limitations [10] of the nanostructures we have achieved a significant PCA with the present combination. Since nanoneedles were grown on the thin film which is on the polymeric fibrous mat, they may not be easily dislodged without a significant mechanical fatigue. This makes them easier to handle and recycle in aqueous environment unlike the case with nanosized particles [6,14,15,25,32]. Of course one can employ the expensive indium tin oxide/fluorine tin oxide substrate based catalysts [10,33]. As an additional advantage, nanoneedles are bound to the surface of the ZnO film on the polymeric fiber and they are well separated from each other during and after the process in contrast to nanoparticle-based catalysts with a significant drawback of agglomeration.

2. Experimental

2.1. Materials

PAN (M_w: ~150,000) was purchased from Scientific Polymer Products, Inc. N,N-dimethylformamide (DMF, Pestanal, Riedel) was used as a solvent. ALD of ZnO was performed using diethylzinc (DEZn, Sigma–Aldrich) and HPLC grade water (H_2O) as the zinc precursor and oxidant, respectively. For hydrothermal process zinc acetate dihydrate (ZAD, ≥98%, Sigma–Aldrich) and hexamethylene tetramine (HMTA, ≥99%, Alfa Aesar) were used. Methylene blue (MB, Sigma–Aldrich, certified by the Biological Stain Commission) was used as a model organic dye to test PCA of the PAN nanofibers and PAN/ZnO nanofibrous mats. All materials were used without any purification. De-ionized (DI) water is obtained from Millipore Milli-Q system.

2.2. Electrospinning of PAN nanofibers

In brief, we have optimized the PAN concentration (12% (w/v) in DMF) to yield uniform and bead-free nanofibers. Prior to electrospinning, PAN solution was stirred for 3 h at room temperature (RT) to obtain homogeneous and clear solution. Well-stirred solution was taken in a 5 mL syringe fitted with a metallic needle of ~0.8 mm of inner diameter. The syringe was fixed horizontally on the syringe pump (KD Scientific, KDS 101) with a feed rate set to 1 mL/h. A high voltage of 15 kV is applied (Matsusada, AU Series) between the syringe needle and a stationary cylindrical metal collector (wrapped with a clean aluminum foil) located at 12 cm from the end of the tip. The electrospinning process was carried out at ~25 °C and 22% relative humidity in an enclosed chamber.

2.3. Preparation of ZnO seed structure by ALD

ZnO deposition on electrospun PAN nanofibers was carried out at ~200 °C in a Savannah S100 ALD reactor (Cambridge Nanotech Inc.). N_2 was used as a carrier gas at a flow rate of ~20 sccm. 400 cycles were applied via exposure mode (a trademark of Ultratech/Cambridge Nanotech Inc.) in which dynamic vacuum was switched to static vacuum before each precursor pulse. This is achieved by closing the valve between the reaction chamber and the pump. After a predetermined exposure time, the vacuum was switched back to dynamic mode for purging excess precursor molecules and gaseous byproducts. One ALD cycle consists of the following steps: valve OFF/N_2 flow set to 10 sccm/H_2O pulse (0.015 s)/exposure (10 s)/valve ON/N_2 purge (20 sccm, 10 s)/valve OFF/N_2 flow set to 10 sccm/DEZn pulse (0.015 s)/exposure (10 s)/valve ON/N_2 purge (20 sccm, 10 s).

2.4. Growth of ZnO nanoneedles by hydrothermal method

ZnO coated PAN nanofibers (PAN/ZnO seed) were used as a seed substrate for the growth of ZnO nanoneedles. ~3.6 mg of PAN/ZnO seed nanofibrous mat was immersed into ~33 mL aqueous solution of equimolar ZAD, HMTA (0.02 M) and mildly stirred overnight at RT. This solution is then heated to 90 °C and kept for 5 h. When the crucible cooled down to RT, the nanofibrous mat was thoroughly rinsed with DI water to remove any residual salts and dried in vacuum oven at ~40 °C for 12 h.

2.5. Characterization techniques

The morphology of the samples was studied using a scanning electron microscope (SEM, FEI–Quanta 200 FEG) with a nominal 5 nm of Au/Pd sputter coating. These images are used to estimate the average fiber diameter (AFD). For transmission electron microscopy (TEM) imaging, samples were sonicated in ethanol for 5 min and the dispersion is collected on holey carbon coated TEM grid. TEM (FEI–Tecnai G2F30) and elemental analysis (energy dispersive X-ray spectroscopy, EDX) was performed on the PAN/ZnO seed nanofibers. Selected area electron diffraction (SAED) patterns of the PAN/ZnO seed nanofibers were also obtained. X-ray diffraction (XRD) patterns from the pristine PAN, PAN/ZnO seed and PAN/ZnO needle samples were collected ($2\theta = 10°–100°$) using PANalytical X'Pert Pro MPD X-ray Diffractometer using Cu Kα radiation ($\lambda = 1.5418$ Å). For surface analysis, samples were subjected to X-ray photoelectron spectroscopy (Thermoscientific, k-Alpha)

under Al Kα ($h\nu$ = 1486.6 eV) line with a charge neutralizer. Pass energy, step size and spot size were 30 eV, 0.1 eV and 400 μm, respectively. Peak deconvolution was performed with Avantage software where the number of peaks was chosen based on the physics of the material while the spectral location and full width at half maximum (FWHM) were allowed to vary. Photoluminescence (PL) measurements were performed using Horiba Scientific FL-1057 TCSPC at an excitation wavelength of 360 nm.

2.6. Photocatalytic activity of the nanofibers

The PCAs of the PAN nanofibers, PAN/ZnO seed and PAN/ZnO needle samples were analyzed through photo induced degradation of MB in aqueous medium (18.8 μM). The nanofibrous mats (weight: 3.6 mg) were immersed in quartz cuvettes containing the MB solution. The cuvettes were exposed to UV light (300 W, Osram, Ultra-Vitalux, sunlight simulation) placed at a distance of ~15 cm. Dye concentrations in the cuvettes were measured using a UV–Vis-NIR spectrophotometer (Varian Cary 5000) at regular time intervals. The nanofibrous mats were pushed to the bottom of the cuvettes during the UV–Vis spectroscopy. The weight of PAN/ZnO seed sample before and after the needle growth was ~3.6 mg and ~3.9 mg respectively which is equivalent to an increase of ~8 wt%. Then the weight of PAN/ZnO needle sample was corrected to equate PAN/ZnO seed sample (3.6 mg). Hence the 3.6 mg of PAN/ZnO needle was found to contain 3.32 mg of seed and 0.28 mg of needles. The rate of dye degradation was quantified via first order exponential fit ($y = y_0 + Ae^{-x/t}$) for each data set. This fit was performed under automated routine with Origin 6.1, where all the parameters are set as free until convergence. We have also repeated the PCA experiment twice (i.e. 2nd and 3rd cycles) for PAN/ZnO needle sample (~3.3 mg) to determine the reusability versus performance.

3. Results and discussion

ZnO nanoneedles were hydrothermally grown on the ZnO seed-coated polymeric nanofibers which were fabricated through combining electrospinning and ALD. The process for fabricating the hierarchical polymer/ZnO nanofiber is illustrated in Fig. 1 and various steps are annotated on the image.

The representative SEM images of PAN nanofibers are given in Fig. 2(a1 and 2). The nanofiber morphology was optimized against several PAN concentrations (results not shown here). About 12% (w/v) was found to be the optimum for the chosen parameters yielding bead-free morphology with an AFD of ~655 ± 135 nm. In electrospinning, it is very typical to obtain fibers in a range of diameters as reported by us [34,35] and many others [36,37]. A close inspection of the morphology reveals a texture like structure, which is sometimes observed for certain electrospun polymeric nanofibers due to the type of solvent used [36–38]. These nanofibers were employed for the second step of seeding with ALD [39–41] by applying 400 cycles at 200 °C using exposure mode (Section 2.3). After the ALD process, we have recorded the SEM images which are shown in Fig. 2(b1 and 2) where the AFD is ~715 ± 125 nm. This measurement suggested an increase in AFD because of ALD coating. The fiber structure was not destroyed during the ALD process where a well defined and stable fiber structure suggests the suitability of the chosen parameters. It is important to point out the need of compatibility between the precursor and polymer as the former can degrade the latter by chemically reacting with it; see the case with ALD processing of Al_2O_3 [42]. On the other hand, in the case of poly(propylene) fibers Al_2O_3 base layer is employed to deposit ZnO, where the former protects the diffusion of DEZn into the polymer [43]. Despite these limitations, ALD coating can yield coral [44], core–shell [45] like complex nanostructures. Such structures are potential for photocatalytic applications [46]. In the present case the morphological changes are similar to our earlier observation [1,2]. It is clear from the image (Fig. 2(b2)) that the surface roughness is increased after ALD process, which is most probably due to the grainy structure of ZnO [1,2]. In our earlier investigation [2], we have shown the grain formation under ALD for different stages of processing cycles. The closely and uniformly packed grains acted as the seed layer for the subsequent growth of nanoneedles of ZnO in hydrothermal process. Note that this grainy structure is not undesired, on the other hand it helps to enhance the PCA, where we can expect the formation of depletion layer within the grain boundaries [47,48]. Such depletion layers are extremely helpful and we will address them in the context of PCA latter in this article. Subsequently, the hydrothermal method was employed to grow ZnO nanoneedles on the ZnO seed-coated polymeric nanofibers. Fig. 2(c1 and 2) shows the representative SEM images of the resulting nanoneedle assemblies (PAN/ZnO needle). It can be seen that nanoneedles cover the surface of the ZnO seed-coated PAN nanofibers. The nanoneedles were straight and no branching was observed. Branching generally occurs because of the irregularity in the seed where it can promote the growth of more than one needle. Notably, in the present context the seeds grown through ALD-process were uniform and did not initiate or support multi-needle growth. SEM images of PAN/ZnO needles at different magnifications are given in Fig. S1 of Supporting Information. By analyzing the SEM images we have estimated the average diameter and length of the nanoneedles to be ~25 nm and ~600 nm, respectively (Fig. 2(c2)). Detailed discussion on the mechanism of the growth of ZnO nanoneedles can be found in the literature [15]. Seeding of ZnO with ALD process and subsequent hydrothermally grown nanorods of ~50 nm diameter with a length of ~0.5–1 μm can be seen in the literature [49,50].

The morphologies of the PAN/ZnO seed nanofibers were further investigated by TEM and shown in Fig. 3(a1). The conformal coating of ZnO can be evidenced from the image with a uniform thickness (~50 nm) in spite of the relatively large surface area of the nanofibers. Notably this supports the earlier argument on uniformity of the grains which are not favorable for multi-needle growth. ALD is well suitable for the high surface area substrates such as a non-woven nanofibers mat as shown by us earlier [1,2]. Growth of ZnO on the PAN nanofibers was calculated to be ~1.25 Å/cycle in the present ALD conditions. In our previous study [1] we observed that ALD of ZnO with 0.015 s pulses and 10 s purges under the dynamic vacuum conditions results in uniform coatings only after a certain number of ALD cycles. In contrast, here we have employed exposure mode (see Section 2.3) which also resulted in a continuous and uniform ZnO coating without the need of high number of ALD cycles. Exposure mode keeps the precursor molecules inside the reaction chamber for a certain period of time which allows them to diffuse into the substrate. The local crystal structure of the ALD-ZnO is investigated through SAED pattern, and shown in Fig. 3(a2). The pattern reveals the polycrystalline nature of ZnO seed. Moreover, the bright spots on the polycrystalline diffraction rings indicate the presence of well crystalline grains [2]. Various diffracted planes are annotated on the image and are consistent with the literature [20,21]. EDX analysis (Fig. S2 of Supporting Information, left panel) on the PAN/ZnO seed nanofibers has shown zinc, oxygen, carbon, nitrogen and copper (from TEM grid) elements. Zn and O originate from ZnO seed, whereas C and N are due to the polymeric core structure of PAN. Also the quantification (Fig. S2 of Supporting Information, right panel) of Zn and O atomic percentages suggests that the material is nominally oxygen rich, within the detection limit of EDX. This is because of the very high surface area yielding defective sites (oxygen vacancies) where molecular oxygen can be adsorbed. It is notable that oxygen vacancies are typical for ZnO in other processing techniques as well, which were determined through an indirect method [19–21,48]. We will see

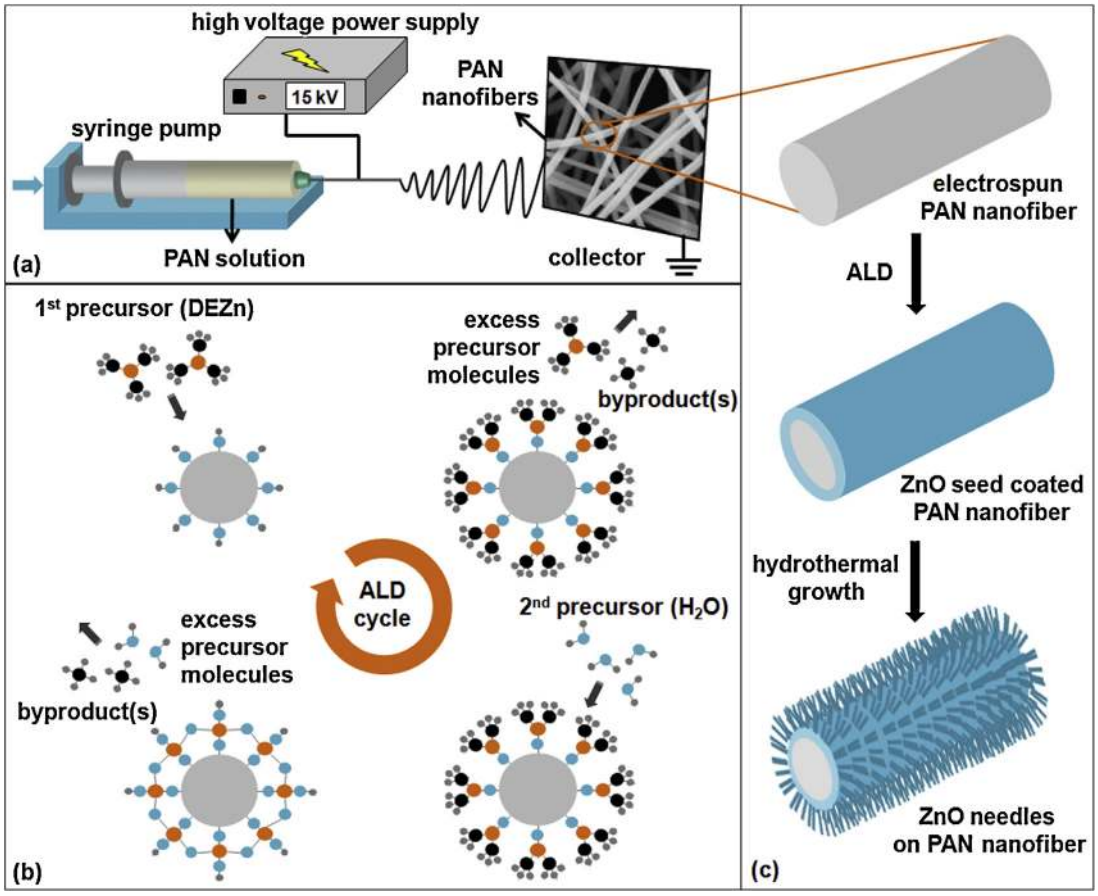

Fig. 1. Schematic representations of (a) electrospinning of PAN solution, (b) ALD of ZnO seed onto PAN nanofiber, and (c) fabrication process for hierarchical PAN/ZnO needle nanofiber.

that the oxygen deficiency is consistent with the PL of ZnO. Furthermore, HRTEM image demonstrated a single crystalline nature of ZnO nanoneedles (Fig. 3(b1)). The lattice spacing was measured to be ~0.525 nm corresponding to the *c-axis* of ZnO, which is the preferential growth direction of the nanoneedles. It is important to determine the growth direction where the polar planes of ZnO have shown to depict relatively higher PCA [13]. The fast Fourier transform (FFT) image is shown in Fig. 3(b2) also demonstrates the single phase [32] structure.

The XRD patterns of pristine PAN, PAN/ZnO seed and PAN/ZnO needle nanofibers are shown in Fig. 4. The XRD pattern of pure PAN nanofibers shows a peak at ~16.93° corresponding to orthorhombic PAN (1 1 0) reflection [51] with an FWHM of ~2.282°. Also a broad and less intense peak-like structure can be seen in the range of 20–30° which corresponds to the (0 0 2) reflection of PAN [52]. After the ALD process the (1 1 0) plane has shown a significant reduction in the FWHM (to ~0.761°) and the broad peak (2θ = 20°–30° indicated with '*' on the image) has stabilized at ~29.69° and became more sharp (FWHM ~0.776°). This is because of the reorganization of the polymeric chains at ~200 °C (ALD processing temperature) equivalent to typical annealing. Furthermore, since the nanoneedles were grown at slightly elevated temperature (~90 °C) for substantial period of time, there is a nominal increase in the FWHM of the PAN diffraction peaks ((1 1 0) and (0 0 2)) because of the incompatible processing temperature. However the relative intensity of this peak was considerably subdued because of the ZnO nanoneedles.

Moving onto the peaks corresponding to the ZnO, we have annotated the reflections on the image for the samples PAN/ZnO seed, and PAN/ZnO needle (Fig. 4a). PAN/ZnO seed and needle samples exhibited diffraction peaks of hexagonal wurtzite structure of ZnO (ICDD 01-074-9940) revealing the successful deposition of ZnO seed as well as nanoneedles on electrospun PAN nanofibers by ALD and hydrothermal technique, respectively. The XRD patterns of PAN/ZnO seed and PAN/ZnO needle match with the reference pattern in terms of peak positions. Also these peak positions match with the literature, when ZnO is prepared through different methods [19–21,48]. However, a close observation of (1 0 0), (0 0 2) and (1 0 1) reflections (Fig. 4b) reveal vital information. If we compare the FWHM values of these peaks across seed and needle samples, we can see that the former is less crystalline than the latter. There is also a shift in the position of the peaks towards higher 2θ value upon needle formation. For the diffraction pattern of PAN/ZnO needle, we can see a shoulder-like structure (denoted with s in Fig. 4b) which corresponds to the PAN/ZnO seed, while a more intense peak corresponding to the highly crystalline ZnO nanoneedle. Peak shift is generally associated with the residual stress (defect-induced) in the material. The stress might be originated from the oxygen vacancies in the lattice [25] or the substrate (PAN nanofibers) [53]. Since the peak shift is noticed for (1 0 0), (0 0 2) and (1 0 1) reflections we can expect that the sample is under compressive strain in the said crystal directions [53]. Notably, the XRD pattern of PAN/ZnO seed is consistent with SAED pattern. Furthermore, the intensity ratios of (0 0 2) polar plane to (1 0 0) nonpolar plane is estimated and it turns out to be the case that seed (~0.78) sample has large fraction of polar planes than needle (~0.65) sample, where larger fraction indicates possibly higher PCA [15]. In this context, it is notable that the XRD is a statistical average of planes from surface as well as subsurface regions. Hence, there is a possibility that the polar planes may be exposed to the surface to enhance the PCA.

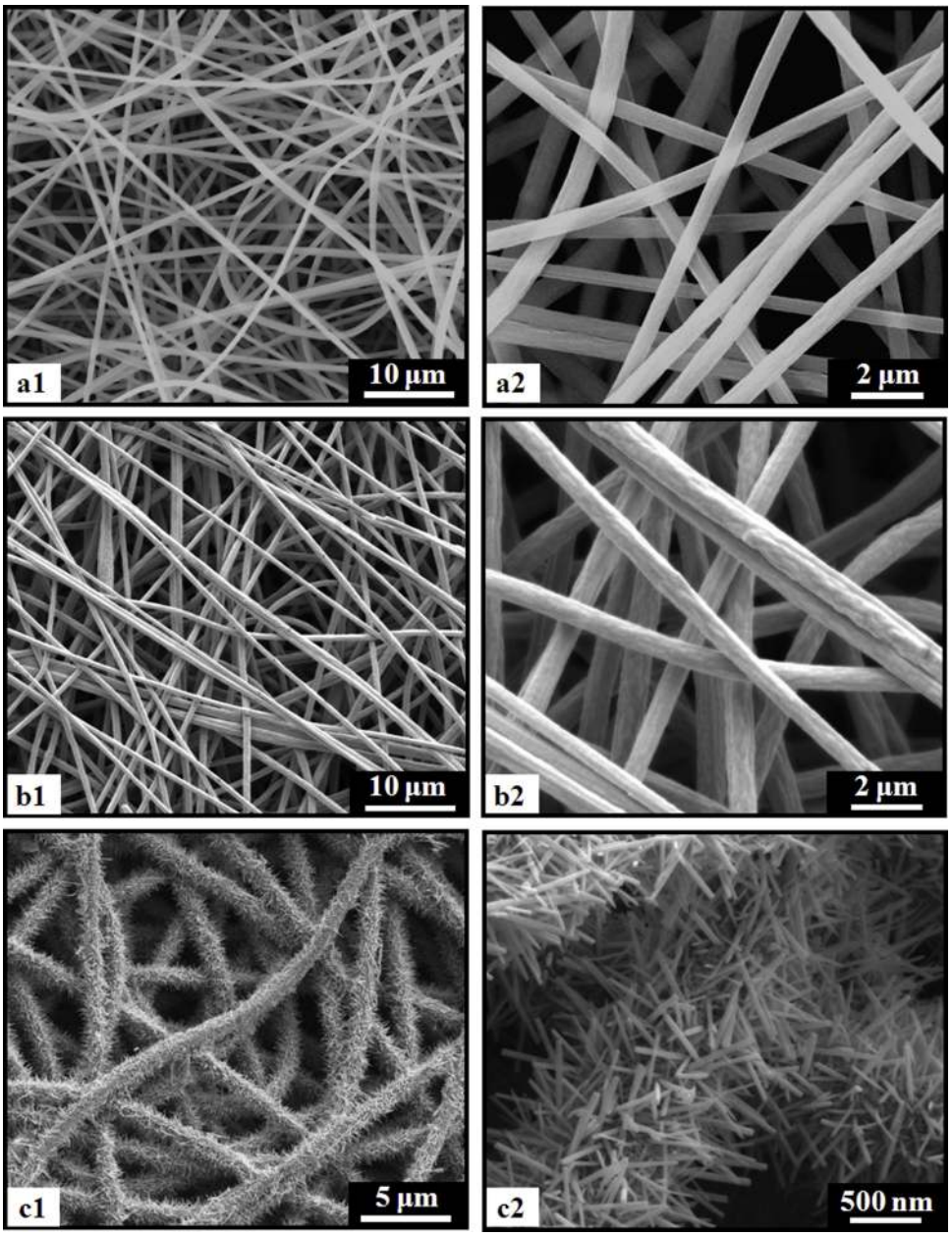

Fig. 2. Representative SEM images of (a1 and 2) pristine PAN, (b1 and 2) PAN/ZnO seed, and (c1 and 2) PAN/ZnO needle nanofibers at different magnifications.

The ionic state of oxygen generally determines the optical emission properties in visible region [19–21] (associated with oxygen related defects) and hence the photocatalytic properties [3,4,13–15]. The O1s XPS spectrum can be deconvoluted into two peaks as shown in Fig. 5, with the peak positions annotated on the image. The peak at ~530.5 eV corresponds to the oxygen in ZnO, which is nominally at the same spectral position for both the samples. The other peak seen at ~531.8 eV and ~532.2 eV for seed and needle sample respectively corresponds to the chemisorbed oxygen of two different chemical origins. The peaks at 531 eV and 531.5 eV are attributed to O^{-x} ions (O^{-} and O^{-2} ions) in the oxygen deficient regions, while peaks at 532.3 eV and 532.7 eV are generally ascribed to the presence of oxygen related species such as –OH, –CO, adsorbed H_2O or O_2 on the surface of ZnO [25,54,55]. During the hydrothermal growth of the needles, grain boundaries and oxygen deficient regions are exposed to hydroxyl ions. These ions perhaps occupy some of the oxygen deficient regions as reflected with a peak at ~532.2 eV. Apart from the difference in the spectral location, the number density of such occupancies is seen in the area of the peak where for PAN/ZnO seed the area ratio is (~49%) significantly higher than needle case (~22%). It is notable that the signal from PAN/ZnO seed sample can be attributed to the sample directly without any ambiguity, however, for the PAN/ZnO needle case, it can be an integral spectrum of seed as well as needle. Despite the latter ambiguity, the above given interpretation is still well applicable and we will see that it is in line with optical and PCA measurements. Finally, a large oxygen-deficient state of the surface layer [25,54] can be seen for PAN/ZnO seed, while in contrast, PAN/ZnO needle sample has shown significantly less oxygen vacancies. Needles resulted in a more stable ZnO enrichment on PAN nanofibers when compared to PAN/ZnO seed [54].

The valence band spectra for PAN/ZnO seed as well needle is shown in Fig. S3 of Supporting Information, where the intensity axis is normalized against the maximum counts and plotted with reference to the binding energy in eV. In zinc oxide, the conduction band (CB) and the valence band (VB) are formed from O1s and Zn2p

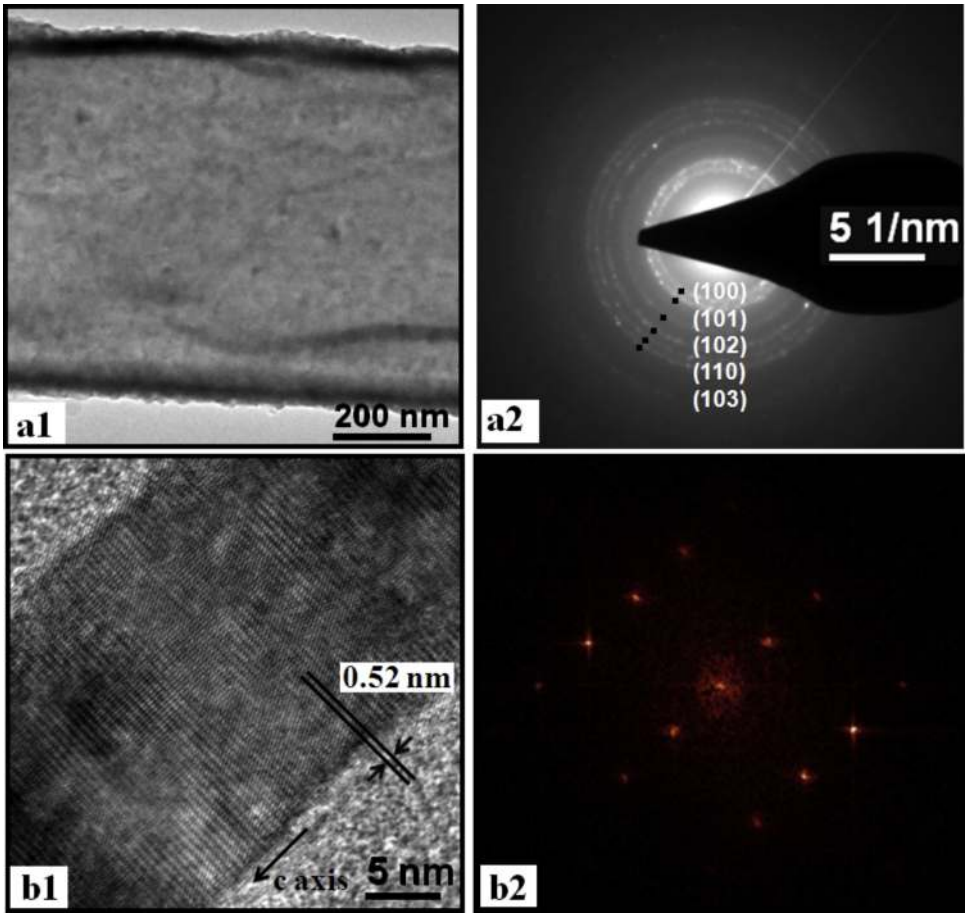

Fig. 3. Representative (a1) TEM image and (a2) SAED pattern of PAN/ZnO seed nanofibers; (b1) HRTEM image and (b2) FFT image of ZnO needle.

orbitals, respectively. As a whole, both the samples have shown the density of states which are typical to zinc oxide [25]. Also the features and their spectral location for both the samples are exactly retraced (Fig. S3 of Supporting Information). This is in contrast to an earlier observation [25] in which V_Os have shown to induce a band gap narrowing by expanding the minimum of CB. However, here the V_Os did not induce any such tailing of CB though evidenced in O1s XPS analysis. The energetic location of oxygen vacancy defects within the band gap will be discussed in the context of PL.

As mentioned earlier, the surface defects play a crucial role in determining the PCA; we can infer the information about such defects through PL spectroscopy. The PL spectra of PAN/ZnO seed and PAN/ZnO needle nanofibers shown in Fig. 6a were obtained at RT. As shown in earlier investigations [19,21,48], the visible emission from ZnO can be decomposed (fittings not shown) into various plausible transitions which will be discussed as we go along. It is known that the typical excition emission band lies in the UV region for ZnO, while the defect related emission in the visible region [19–21,47,48,56]. Based on the literature the possible transitions and the corresponding emission wavelengths are schematized in Fig. 6b, which are cross-annotated on Fig. 6a with arrows on the wavelength axis.

We start with the peaks corresponding to the interband transition (excitonic recombination) which is the least controversial emission. As expected, relatively better crystalline PAN/ZnO needle has shown a clear peak at ~3.25 eV, while in contrast, only a signature of such emission is noticed for PAN/ZnO seed sample. This emission peak is consistent with the literature in terms of spectral location [21], yielding a band gap of 3.31 eV [21] when an excition binding energy of 60 meV is assumed. The relative intensity of this interband transition is enhanced upon needle formation on ALD seed layer, which suggests an improvement in the overall optical quality of the material. In the literature [18,64,65], we can see needle/rod like structure, however, the samples depicted broad near UV emission and almost negligible visible emission. However, in contrast, we have comparatively sharp UV emission and significant visible emission, where we are aimed to harness the defect related PCA. Note that the emission from PAN/ZnO needle is the integral response of two components, one of which is from the needle itself, while the other is from PAN/ZnO seed. As PAN/ZnO seed did not show any clear excition emission, the peak seen in needle sample arises from the ZnO-nanoneedle. In the case of PAN/ZnO seed because of the large grain boundaries from the film like structure on the cylindrical peripheral, a significant amount of surface recombination takes place giving the predominant visible emission. Various plausible emissions are schematized in Fig. 6b and shown with numerals (1) though (7) where the energetic locations of the defects have been obtained from the corresponding references; (1) [57], (2) [58], (3) [59,60], (4) [61], (5) [47,48], (6) [62] and (7) [63]. Violet emissions centered at about 410 nm are broader, and not as prominent as green emission centered around 520 nm, which were interpreted to be related to the defects such as zinc interstitials (Zn_i) and V_Os, respectively. Violet emission can result from an integral response of three transitions [57–60] as denoted on Fig. 6b with A through E. In the visible region of the spectrum, both the samples have exhibited a broad emission which is again an integral response of the defects of two different origins. Also, a slight though noticeable blue shift can be noticed in the center of the peak (peak positions are annotated on the image) for PAN/ZnO needle from its seed counterpart. Although the variation is nominal

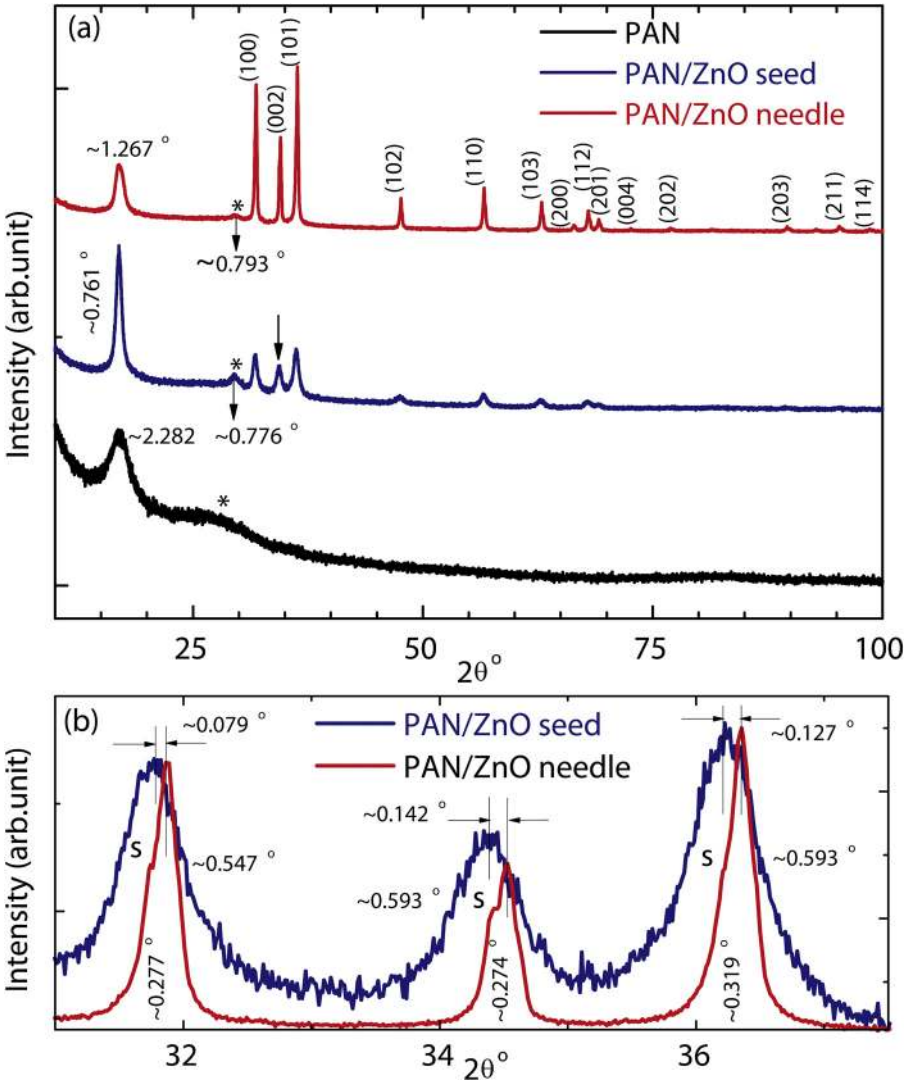

Fig. 4. (a) XRD patterns of nanofibers of PAN, PAN/ZnO seed and PAN/ZnO needle, and (b) magnified XRD patterns in the range of 31–37.5°.

(~0.02 eV), when it comes to the density of the defects, it plays a crucial role in determining the PCA of the material. The optical quality of the semiconductor can be estimated by taking the intensity ratios of UV to visible emission [19–21]. It is worth noting that the ratio of the intensity of band to band transition (~381 nm) to the intensity of the defect level emission (~520 nm) is ten times higher for the PAN/ZnO needle than PAN/ZnO seed. This high ratio indicates higher optical quality of the PAN/ZnO needle sample. Unlike the violet emission, green emission is slightly complex [47,48]. In the bulk grain region (BGR) singly positively charged V_O captures an electron from CB and forms a neutral V_O (i.e. $V_O^+ \rightarrow V_O^*$). In the depletion region (DR) if the singly positively charged V_O captures a hole from the VB, it forms doubly positive V_O (i.e. $V_O^+ \rightarrow V_O^{++}$). Hence, the green emission is a combination of transitions from V_O^* to the VB and CB to V_O^{++} emitting F and G wavelengths, respectively (Fig. 6b) [47,48]. Also, relatively lower intense interband emission suggests that the photo-generated electrons and holes are captured by V_O^+ emitting photons in the visible region of the spectrum. This interpretation will be employed to explain the PCA of the samples.

We have comparatively investigated the PCA of PAN nanofibers, PAN/ZnO seed and PAN/ZnO needle by analyzing the time dependent decomposition of MB in aqueous medium under illumination. To evaluate the degradation rate of MB, its characteristic absorption peak (~665 nm) is monitored against UV-exposure time. The rate of degradation is defined as C/C_o where C_o and C represent the initial concentration of MB before and after irradiation at a given time respectively. The pristine PAN nanofibers are porous to adsorb (not degrade) the dye up to a noticeable level (results not shown) until equilibrium between adsorption and desorption is attained. Hence we have taken the surface adsorption as reference and analyzed the PAN nanofibers effect on dye degradation, where no effect is seen (Fig. 7a). This is consistent with the literature [66]. On the other hand, it is notable that ALD unveils conformal coating on electrospun nanofibers and hence the exposure of PAN nanofibers directly to the dye can be very unlikely. In the case of PAN/ZnO seed and needle cases we have observed a nonlinear behavior, and the electron transfer between donor states and the dye governs the degradation ratio [67,68]. Hence we have addressed the nature of degradation in the context of each sample independently. When the catalysts are immersed in the MB solution, the PCA with respect to UV irradiation time is depicted in Fig. 7a along with the pristine MB solution which was subjected to the same UV treatment. According to the Langmuir–Hinshelwood model the exponential relationship of (C/C_o) against time indicates that MB degradation follows pseudo-first-order kinetics. We have performed exponential fit to the each data set and the decay constants are given on the figure.

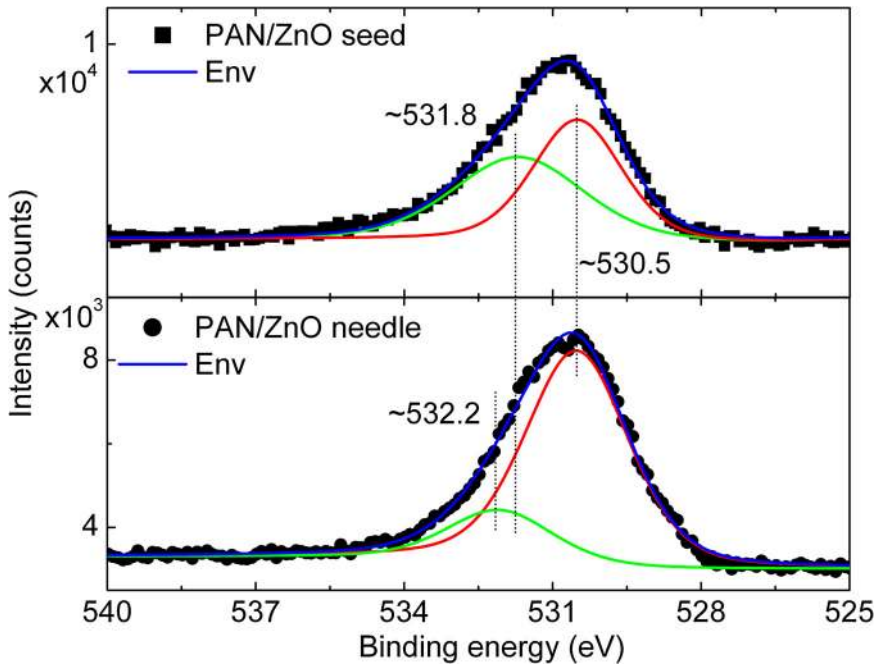

Fig. 5. Peak deconvolution of core-level XPS spectra of O1s from PAN/ZnO seed and PAN/ZnO needle samples. The spectral locations of the peaks are annotated on the image.

In the case of UV exposure to pristine solution the data has shown decay constant of ~157 min. Notably though to the naked eye, the degradation of the MB (without nanofibers) is not clearly observed upon exposure to UV radiation for 210 min (see Fig. S4 of Supporting Information for digital photographs). For PAN/ZnO seed, ~47% of MB decomposed in nominal 60 min yielding a degradation rate of ~113 min. An improvement of ~28% is noticed when compared to the degradation rate in the case of no catalyst. Eventually, the blue solution was almost decolorized after ~210 min of UV irradiation (Fig. S4 of Supporting Information). In the case of PAN/ZnO needle, the decomposition of MB was ~93% in ~60 min. Interestingly, in the case of PAN/ZnO needles, at a degradation rate of ~15 min has shown improvement of ~91% and ~87% for no catalyst and PAN/ZnO seed samples, respectively. PCA was

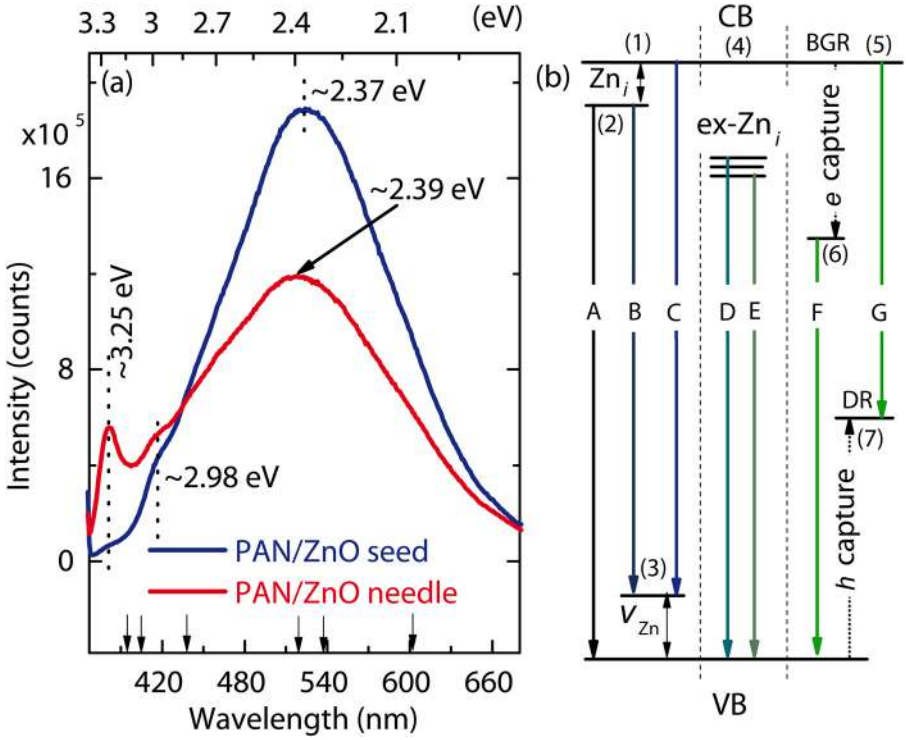

Fig. 6. (a) PL spectra of PAN/ZnO seed and needle counterpart, and (b) depicts various crystal defects and possible transitions [21]. The energetic location of each defect level (denoted by numerals) is obtained from the corresponding references (1) [57], (2) [58], (3) [59,60], (4) [61], (5) [47,48], (6) [62] and (7) [63]. The alphabets stand for emission energies in nanometer, where $A = 395$, $B = 437$, $C = 405$, $D = 440$, $E = 455$, $F = \sim 500$, and $G = 564$. V_{Zn} is located 0.30 eV above the VB, while Zn_i is at 0.22 eV below the CB. In the bulk grain region (BGR) and in the depletion region (DR) $V_O^+ \rightarrow V_O^*$ and $V_O^+ \rightarrow V_O^{++}$ processes take place, respectively.

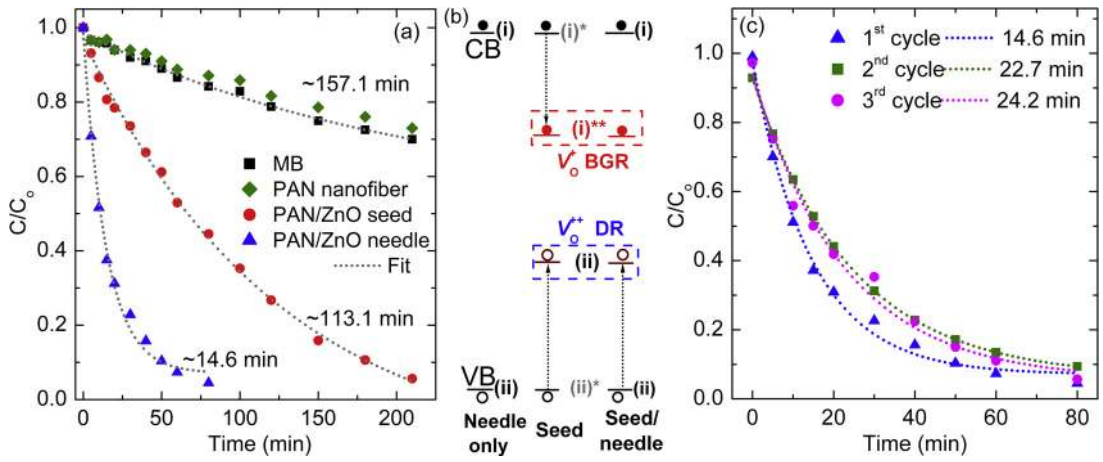

Fig. 7. (a) Degradation rate of MB in aqueous environment tested for pristine, in the presence of PAN nanofibers, PAN/ZnO seed and PAN/ZnO needle (1st cycle) cases, (b) plausible mechanism of photocatalysis involving oxygen vacancies, where (i) and (ii) stand for processes acceptor → acceptor$^-$ and donor → donor$^+$ respectively, and (c) PCA of PAN/ZnO needle nanofibers for 1st, 2nd and 3rd cycles.

relatively higher for the PAN/ZnO needle than PAN/ZnO seed, which is because of not only relatively higher surface area but also its higher crystal quality of the needle-morphology. As pointed in Section 2.6, ZnO-seed content in PAN/ZnO needle sample is less than PAN/ZnO seed, where the needles compensate the remainder of the weight. Although the needles are about 0.02 mg in PAN/ZnO needle they show significant effect on PCA. As an aside the improvement in the surface area is about 30 times, where ~1200–1500 needles are approximated on fiber (~800 nm and 715 nm of length and diameter respectively). In our previous study [2] high density nanoparticles have shown ~1.2 times higher PCA than nanocoating case. It needs to be emphasized that within this study we have achieved an improvement of dye degradation rate of nearly 8 times for needle case when compared to seed case. In the following, we establish the argument for PCA and latter correlate with each of the samples. Under suitable illumination electrons can be excited from the VB to reach the CB, leaving behind holes in the VB [21,48]. If these separated charges can migrate to the surface of the semiconductor before they recombine, then they have a chance to participate in the redox reactions [69]. Formation of hydroxyl radical ($^{\bullet}$OH) is the key for the PCA, in which holes [70] as well as electrons (which may be captured by molecular oxygen forming superoxide anions [71], $^{\bullet}O_2^-$) are involved at VB and CB, respectively. Because of the presence of highly oxidative hole as well as $^{\bullet}$OH radicals the organic dye can be decomposed either partially or completely. We have shown the possible mechanism [10,70,71] in Fig. S5 of Supporting Information. In the literature [10,72], it is discussed that PCA takes place at the VB and the defect state (formed either by doping [72] or intrinsic [10] e.g. V_Os), where the latter captures a free electron from the CB. However, under illumination, O_2 can capture an electron from CB promoting the PCA. The basis for this argument is the interband transition seen in the PL spectrum from PAN/ZnO needle sample which suggests a possibility of photo-electrons recombining with holes in CB, bypassing the defect state. Hence, at a given time, under illumination electrons are populated in CB to be captured by O_2. On the other hand, the photo-electrons can also be captured by O_2 at V_Os producing superoxide radical anions. It is also shown earlier that the V_Os can act as active sites for PCA in ZnO nanostructures [13,25,73]. Since the V_Os are located on the surface (interfaces of the grains and depletion regions) [47,48] they directly involve in PCA [74]. Notably, V_O is treated as electron acceptors [74] by capturing an electron from CB [21,47,48] and hence the recombination process is delayed [10]. In the PCA at heterojunction (e.g. ZnO/ZnSe [32], ZnO/Cu_2O [33]) (i) acceptor → acceptor$^-$ and (ii) donor → donor$^+$ processes occur at CB of ZnO and VB of ZnSe (or Cu_2O), respectively, where the charge migration across the heterojunction delays the recombination process. In the context of Pt–ZnO nanocomposite [74], a well defined emission from interband transition in PL is not seen because of the low recombination rate of e/h pairs which is induced by Pt.

In the background of the above discussion, for a hypothetical case of virtually defect free nanoneedle (i.e. high optical quality, Fig. 7b, needle only), PCA is because of (i) and (ii) processes taking place at CB and VB of ZnO nanoneedle respectively. In the case of PAN/ZnO seed, there is just a signature of interband transition in PL, hence the PCA that takes place at CB and VB is not dominant, which is denoted with (i)* and (ii)*, respectively (Fig. 7b, seed). The defect site V_O^+ is located in the bulk of the grain [19,21,47,48] (Fig. 6b) and hence it is not accessible for PCA, unless the captured electron migrates to the surface. This may be a very unlikely case as these states are highly localized. Furthermore, the PCA associated with V_O^+ is relatively weak and is denoted with (i)**. In contrast, the defect site V_O^{++}, which is located in the depletion region (e.g. grain boundaries [19,21,47,48], Fig. 6b), is well accessible for PCA and is denoted with (ii). In principle, the present ALD grown ZnO film is evidenced to be grainy with large portions of grain boundaries. For PAN/ZnO needle case, the PCA is an integral effect of V_Os ((ii), from PAN/ZnO seed sample) as well as the catalysis taking place at CB (i) and VB (ii) of needle (Fig. 7b, seed/needle). The combined effect of all these processes yielded significantly higher PCA. We have also seen that the seed sample has large fraction of polar planes than needle sample (analysis from XRD), hence it is expected [15] that seed sample should have shown better PCA. Although it appears to be not the case here, a careful understanding of the both materials reveals that the present results are in line with Ref. [15]. It is well agreed that the sample with larger fraction of polar planes yield higher PCA (owing to their V_Os) what we see is a synergy effect of the needle and the seed, hence these results are not in contrast to an earlier observation [15].

The structural durability of the PAN/ZnO seed and PAN/ZnO needle nanofibers was also examined through SEM after the photocatalysis (Fig. S6 of Supporting Information). We note that the stability as well as durability plays a vital role because of their potential application in water purification of the organic pollutants. As outlined in the introduction, we characterize the material in terms of their catalytic efficiency and durability with reference to recycling. We have repeated the PCA experiment twice for the PAN/ZnO needle (Fig. 7c). There is a slight decrease in the efficiency of PCA from 1st cycle to the following cycles, where the 1st cycle has shown ~93% in ~60 min of UV irradiation (Fig. 7c).

The deterioration could have occurred from various factors. Firstly, a small quantity (~0.3 mg) of nanofibrous mat was used for SEM analysis after the 1st cycle, leaving behind less amount of catalytic material for the 2nd and 3rd cycles. Secondly, by considering the SEM images of the latter cycles (after 1st cycle, Fig. S6b; after 3rd cycle, Fig. S6c of Supporting Information), it is clear that the density of nanoneedles is decreased to a certain degree. This is because of the mechanical fatigue while inserting the nanofibrous mat through a tiny hole of the cuvette and UV–Vis spectroscopy. If the nanofibrous mat has been handled carefully then we believe that the performance of catalyst after the 2nd cycle will be as good as or at least comparable with that of a fresh sample.

4. Conclusions

Here we have reported the results of an investigation on ZnO-based photocatalyst synthesized on electrospun PAN nanofibers. This catalyst harnesses PCA at three different energetic locations within the band gap of ZnO, namely, oxygen vacancy sites, VB and CB. In order to achieve this, morphologically well defined PAN nanofibers are produced via electronspinning, followed by ALD to deposit ZnO in a well controlled manner yielding a thin and conformal coating on the nanofibers. The last step consists of hydrothermal growth of ZnO single crystal needle like structures on the ALD seed coating. The present investigation also re-iterates the flexibility of various techniques and a combination of ALD and hydrothermal growth. The ALD parameters are optimized in such a way that the seeds do not initiate multi-needle growth which in turn improves the subsequent processing of hydrothermal growth as in the present case or other methods such as sol–gel. The structural investigation (XRD) revealed the stress related information of the wurtzite structured PAN/ZnO seed as well as PAN/ZnO needle. The stress in the material might have been originated due to the polymeric nanofibrous substrate and the associated high surface area. Investigation on local crystal structure (TEM) also supported the wurtzite structure and hinted oxygen deficiency in ALD-ZnO. However, as expected hydrothermally grown ZnO happened to be in single crystalline state and no multiple phases were observed in the FFT image. The origin of the defect and the oxygen deficiency can be identified with XPS rather precisely, where we have noticed that PAN/ZnO seed sample consists of O^{-x} type ions, while PAN/ZnO needle sample consists of –OH, –CO, H_2O, or O_2 adsorbed at the defect site. The former further supports the existence of grain boundaries in the PAN/ZnO seed and less defective PAN/ZnO needle. Being very crucial for PCA, the results from PL suggested an oxygen deficient PAN/ZnO seed while the PAN/ZnO needles of relatively better optical quality. We note the consistency between the PL and XPS measurements. Based on the literature, various emission bands have been ascribed to their plausible origin. We have suggested a mechanism for the improved PCA of PAN/ZnO needle sample, when compared with PAN/ZnO seed. We have interpreted the PCA in conjunction with PL, where we point out the fact that oxygen vacancy captures a hole from the CB and hence the recombination process is delayed. Also this captured hole can take part in PCA as it is located within the grain boundary region. The improvement is attributed to the collective effect which enabled the active participation of defect state and the catalysis taking place at CB as well as VB. If photocatalysis consists of only defect related activity, or that takes place at CB and VB is not sufficient to achieve higher PCA. On the other hand, the discussion on PCA assumes that the surface defects on nanoneedles are negligible at an acceptable level by given its crystallinity, and the relative intensity of visible emission has in fact subdued when compared to the UV emission. Furthermore, the samples are subjected to recycling and nominally the PAN/ZnO needle depicted a comparable performance with the fresh sample. Since the catalyst is synthesized on flexible polymeric nanofibers, the membrane can be handled rather easily (Fig. S7 of Supporting Information). Finally it is convincing that these ZnO nanostructures are well suited and potential candidates for waste water treatment with solar energy where their performance, structural stability and reusability are worth mentioning.

Acknowledgements

S.V. thanks The Scientific & Technological Research Council of Turkey (TUBITAK) (TUBITAK-BIDEB 2216, Research Fellowship Programme for Foreign Citizens) for postdoctoral fellowship. F.K. and C.O.-A. thanks TUBITAK-BIDEB for a PhD scholarship. N.B. thanks EU FP7-Marie Curie-IRG for funding NEMSmart (PIRG05-GA-2009-249196). T.U. thanks EU FP7-Marie Curie-IRG (NANOWEB, PIRG06-GA-2009-256428) and The Turkish Academy of Sciences – Outstanding Young Scientists Award Program (TUBA-GEBIP) for funding. Authors thank M. Guler for technical support for TEM analysis.

Appendix A. Supplementary data

Supplementary data associated with this article can be found, in the online version, at http://dx.doi.org/10.1016/j.apcatb.2014.03.004.

References

[1] F. Kayaci, C. Ozgit-Akgun, I. Donmez, N. Biyikli, T. Uyar, ACS Appl. Mater. Interfaces 4 (2012) 6185–6194.
[2] F. Kayaci, C. Ozgit-Akgun, N. Biyikli, T. Uyar, RSC Adv. 3 (2013) 6817–6820.
[3] Z. Pei, L. Ding, J. Hu, S. Weng, Z. Zheng, M. Huang, P. Liu, Appl. Catal. B. 143–143 (2013) 736–743.
[4] T.-T. Chen, I.-C. Chang, M.-H. Yang, H.-T. Chiu, C.-Y. Lee, Appl. Catal. B. 142–143 (2013) 442–449.
[5] H.U. Lee, S.Y. Park, S.C. Lee, J.H. Seo, B. Son, H. Kim, H.J. Yun, G.W. Lee, S.M. Lee, B. Nam, J.W. Lee, Y.S. Huh, C. Jeon, H.J. Kim, J. Lee, Appl. Catal. B. 144 (2014) 83–89.
[6] Y. Zuo, Y. Qin, C. Jin, Y. Li, D. Shi, Q. Wu, J. Yang, Nanoscale 5 (2013) 4388–4394.
[7] M. Pelaez, N.T. Nolan, S.C. Pillai, M.K. Seery, P. Falaras, A.G. Kontos, P.S.M. Dunlop, J.W.J. Hamilton, J.A. Byrne, K. O'Shea, M.H. Entezari, D.D. Dionysiou, Appl. Catal. B. 125 (2012) 331–349.
[8] S. Hotchandani, P.V. Kamat, J. Phys. Chem. 96 (1992) 6834–6839.
[9] N. Chouhan, C.L. Yeh, S.-F. Hu, R.-S. Liu, W.-S. Chang, K.-H. Chen, Chem. Commun. 47 (2011) 3493–3495.
[10] F. Xu, Y. Shen, L. Sun, H. Zeng, Y. Lu, Nanoscale 3 (2011) 5020–5025.
[11] D.-X. Xu, Z.-W. Lian, M.-L. Fu, B. Yuan, J.-W. Shi, H.-J. Cui, Appl. Catal. B. 142–143 (2013) 377–386.
[12] M.R. Hoffmann, S.T. Martin, W. Choi, D. Bahnemann, Chem. Rev. 95 (1995) 69–96.
[13] J. Wang, P. Liu, X. Fu, Z. Li, W. Han, X. Wang, Langmuir 25 (2009) 1218–1223.
[14] Y. Zheng, C. Chen, Y. Zhan, X. Lin, Q. Zheng, K. Wei, J. Zhu, Y. Zhu, Inorg. Chem. 46 (2007) 6675–6682.
[15] G.R. Li, T. Hu, G.L. Pan, T.Y. Yan, X.P. Gao, H.Y. Zhu, J. Phys. Chem. C 112 (2008) 11859–11864.
[16] X. Liu, L. Pan, T. Lv, Z. Sun, C. Sun, RSC Adv. 2 (2012) 3823–3827.
[17] V. Subramanian, E.E. Wolf, P.V. Kamat, Langmuir 19 (2003) 469–474.
[18] T.J. Athauda, U. Butt, R.R. Ozer, RSC Adv. (2013), http://dx.doi.org/10.1039/c1033ra43672a.
[19] S. Vempati, A. Shetty, P. Dawson, K. Nanda, S.B. Krupanidhi, J. Cryst. Growth 343 (2012) 7–12.
[20] S. Vempati, A. Shetty, P. Dawson, K.K. Nanda, S.B. Krupanidhi, Thin Solid Films 524 (2012) 137–143.
[21] S. Vempati, J. Mitra, P. Dawson, Nanoscale Res. Lett. 7 (2012) 470.
[22] D. Chu, Y. Masuda, T. Ohji, K. Kato, Langmuir 26 (2010) 2811–2815.
[23] N. Kislov, J. Lahiri, H. Verma, D.Y. Goswami, E. Stefanakos, M. Batzill, Langmuir 25 (2009) 3310–3315.
[24] T.J. Sun, J.S. Qiu, C.H. Liang, J. Phys. Chem. C 112 (2008) 715–721.
[25] S.A. Ansari, M.M. Khan, S. Kalathil, A.N. Khan, J. Lee, M.H. Cho, Nanoscale 5 (2013) 9238–9246.
[26] N. Scharnagl, H. Buschatz, Desalination 139 (2001) 191–198.
[27] S. Yang, Z. Liu, J. Membr. Sci. 222 (2003) 87–98.
[28] L. Zhang, J. Luo, T.J. Menkhaus, H. Varadaraju, Y. Sun, H. Fong, J. Membr. Sci. 369 (2011) 499–505.
[29] Y. Mei, C. Yao, K. Fan, X. Li, J. Membr. Sci. 417 (2012) 20–27.
[30] X. Zhang, V. Thavasi, S.G. Mhaisalkar, S. Ramakrishna, Nanoscale 4 (2012) 1707–1716.

[31] H. Tong, S. Ouyang, Y. Bi, N. Umezawa, M. Oshikiri, J. Ye, Adv. Mater. 24 (2012) 229–251.
[32] S. Cho, J.-W. Jang, J.S. Lee, K.-H. Lee, Nanoscale 4 (2012) 2066–2071.
[33] T. Jiang, T. Xie, L. Chen, Z. Fu, D. Wang, Nanoscale 5 (2013) 2938–2944.
[34] T. Uyar, R. Havelund, J. Hacaloglu, X. Zhou, F. Besenbacher, P. Kingshott, Nanotechnology 20 (2009) 125605.
[35] S. Vempati, J.B. Veluru, R.G. Karunakaran, D. Raghavachari, T.S. Natarajan, J. Appl. Phys. 110 (2011) 113718.
[36] S. Ramakrishna, K. Fujihara, W. Teo, T. Lim, Z. Ma, An Introduction to Electrospinning and Nanofibers, World Scientific Publishing Company, Singapore, 2005.
[37] J.H. Wendorff, S. Agarwal, A. Greiner, Electrospinning: Materials, Processing, and Applications, Wiley-VCH, Germany, 2012.
[38] J.V. Nygaard, T. Uyar, M. Chen, P. Cloetens, P. Kingshott, F. Besenbacher, Nanoscale 3 (2011) 3594–3597.
[39] S.M. George, Chem. Rev. 110 (2009) 111–131.
[40] M. Leskelä, M. Ritala, Angew. Chem. Int. Ed. 42 (2003) 5548–5554.
[41] C. Detavernier, J. Dendooven, S.P. Sree, K.F. Ludwig, J.A. Martens, Chem. Soc. Rev. 40 (2011) 5242–5253.
[42] C.J. Oldham, B. Gong, J.C. Spagnola, J.S. Jur, K.J. Senecal, T.A. Godfrey, G.N. Parsons, J. Electrochem. Soc. 158 (2011) D549–D556.
[43] W.J. Sweet, J.S. Jur, G.N. Parsons, J. Appl. Phys. 113 (2013) 194303.
[44] P. Heikkilä, T. Hirvikorpi, H. Hilden, J. Sievänen, L. Hyvärinen, A. Harlin, M. Vähä-Nissi, J. Mater. Sci. 47 (2012) 3607–3612.
[45] E. Santala, M. Kemmel, M. Leskela, M. Ritala, Nanotechnology 20 (2009) 035602.
[46] I.M. Szilagyi, E. Santala, M. Heikkila, V. Pore, M. Kemmel, T. Nikitin, G. Teucher, T. Firkala, L. Khriachtchev, M. Rsanen, M. Ritala, M. Leskala, Chem. Vap. Deposition 19 (2013) 149–155.
[47] J.D. Ye, S.L. Gu, F. Qin, S.M. Zhu, S.M. Liu, X. Zhou, W. Liu, L.Q. Hu, R. Zhang, Y. Shi, Y.D. Zheng, Appl. Phys. A: Mater. Sci. Process. 81 (2005) 759–762.
[48] S. Vempati, S. Chirakkara, J. Mitra, P. Dawson, K.K. Nanda, S.B. Krupanidhi, Appl. Phys. Lett. 100 (2012) 162104.
[49] B. Gong, Q. Peng, J.-S. Na, G.N. Parsons, Appl. Catal. A 407 (2011) 211–216.
[50] A. Sugunan, V.K. Guduru, A. Uheida, M.S. Toprak, M. Muhammed, J. Am. Ceram. Soc. 93 (2010) 3740–3744.
[51] P. Liu, Y. Zhu, J. Ma, S. Yang, J. Gong, J. Xu, Colloid. Surf. A 436 (2013) 489–494.
[52] Z. Zhang, L. Zhang, S. Wang, W. Chen, Y. Lei, Polymer 42 (2001) 8315–8318.
[53] B.D. Cullity, S.R. Stock, Elements of X-ray Diffraction, 3rd ed., Prentice Hall, 2001.
[54] M. Chen, X. Wang, Y. Yu, Z. Pei, X. Bai, C. Sun, R. Huang, L. Wen, Appl. Surf. Sci. 158 (2000) 134–140.
[55] A. Stănoiu, C.E. Simion, S. Somăcescu, Sens. Actuators B: Chem. 186 (2013) 687–694.
[56] A. Djurišić, W.C. Choy, V.A.L. Roy, Y.H. Leung, C.Y. Kwong, K.W. Cheah, T. Gundu Rao, W.K. Chan, H. Fei Lui, C. Surya, Adv. Funct. Mater. 14 (2004) 856–864.
[57] C.H. Ahn, Y.Y. Kim, D.C. Kim, S.K. Mohanta, H.K. Cho, J. Appl. Phys. 105 (2009) 013502.
[58] E.G. Bylander, J. Appl. Phys. 49 (1978) 1188.
[59] B. Lin, Z. Fu, Y. Jia, Appl. Phys. Lett. 79 (2001) 943.
[60] P.S. Xu, Y.M. Sun, C.S. Shi, F.Q. Xu, H.B. Pan, Nucl. Instrum. Meth. B 199 (2003) 286–290.
[61] H. Zeng, G. Duan, Y. Li, S. Yang, X. Xu, W. Cai, Adv. Funct. Mater. 20 (2010) 561.
[62] K. Vanheusden, W.L. Warren, C.H. Seager, D.R. Tallant, J.A. Voigt, B.E. Gnade, J. Appl. Phys. 79 (1996) 7983.
[63] A.V. Dijken, E.A. Meulenkamp, D. Vanmaekelbergh, A. Meijerink, J. Lumin. 90 (2000) 123–128.
[64] T.J. Athauda, P. Hari, R.R. Ozer, ACS Appl. Mater. Interfaces 5 (2013) 6237–6246.
[65] T.J. Athauda, R.R. Ozer, Cryst. Growth Design 13 (2013) 2680–2686.
[66] C. Prahsarn, W. Klinsukhon, N. Roungpaisan, Mater. Lett. 65 (2011) 2498–2501.
[67] S. Baruah, S.S. Sinha, B. Ghosh, S.K. Pal, A.K. Raychaudhuri, J. Dutta, J. Appl. Phys. 105 (2009) 074308.
[68] S.S. Warule, N.S. Chaudhari, B.B. Kale, M.A. More, Cryst. Eng. Commun. 11 (2009) 2776–2783.
[69] N. Daneshvar, D. Salari, A.R. Khataee, J. Photochem. Photobiol. A 162 (2004) 317–322.
[70] R.W. Matthews, J. Catal. 97 (1986) 565–568.
[71] I. Izumi, W.W. Dunn, K.O. Wilbourn, F.R.F. Fan, A.J. Bard, J. Phys. Chem. 84 (1980) 3207–3210.
[72] Y. Yang, Y. Li, L. Zhu, H. He, L. Hu, J. Huang, F. Hu, B. Hec, Z. Ye, Nanoscale 5 (2013) 10461–10471.
[73] J. Wang, Z. Wang, B. Huang, Y. Ma, Y. Liu, X. Qin, X. Zhang, Y. Dai, ACS Appl. Mater. Interfaces 4 (2012) 4024–4030.
[74] C. Yu, K. Yang, Y. Xie, Q. Fan, J.C. Yu, Q. Shu, C. Wang, Nanoscale 5 (2013) 2142–2151.